sustainability

Article

Thermal Radiation and Mass Transfer Analysis in an Inclined Channel Flow of a Clear Viscous Fluid and H_2O/EG-Based Nanofluids through a Porous Medium

K. M. Pavithra [1], B. N. Hanumagowda [1], S. Suresh Kumar Raju [2], S. V. K. Varma [1], Nimer Murshid [3], Hasan Mulki [3,*] and Wael Al-Kouz [3]

[1] School of Applied Sciences, Department of Mathematics, REVA University, Bengaluru 560064, Karnataka, India
[2] Department of Mathematics and Statistics, College of Science, King Faisal University, Al-Ahsa 31982, Saudi Arabia
[3] College of Engineering and Technology, American University of the Middle East, Egaila 54200, Kuwait
* Correspondence: hasan.mulki@aum.edu.kw

Abstract: Nanofluid flow has acquired various interesting dimensions with the advent of several novel approaches to studying thermophysical properties. The present work focuses on a comparative study of clear viscous and nanofluid ($EG - Al_2O_3$, $EG - Zr$, $H_2O - Al_2O_3$, $H_2O - Zr$) flow in a two-phase inclined channel saturated with a porous medium in the presence of thermal radiation, species diffusion, and viscous and Darcy dissipation effects. The controlling equations of the flow model were solved analytically using the regular perturbation technique. The graphical solutions are used to examine the impacts of physical parameters on the most significant flow features. Surface graphs with distinct entrenched parameters represent heat transfer rates and shear stresses on plates. The resulting heat transfer was enhanced by raising the thermal and solute buoyancy strengths, while thermal radiation had the opposite outcome. This enhancement of temperature was maximum for water–zirconium and minimum for ethylene glycol–aluminum oxide nanofluid. The concentration of the entire fluid medium is reduced by decreased mass diffusivity. The enhancement of temperature and velocity is found to be maximum in the nanofluid region and clear fluid region, respectively. This study is validated with previously published works to demonstrate its effectiveness.

Keywords: radiation; chemical reaction; nanofluids; porous medium; viscous; Darcy dissipation; sustainability

Citation: Pavithra, K.M.; Hanumagowda, B.N.; Raju, S.S.K.; Varma, S.V.K.; Murshid, N.; Mulki, H.; Al-Kouz, W. Thermal Radiation and Mass Transfer Analysis in an Inclined Channel Flow of a Clear Viscous Fluid and H_2O/EG-Based Nanofluids through a Porous Medium. *Sustainability* **2023**, *15*, 4342. https://doi.org/10.3390/su15054342

Academic Editor: Cinzia Buratti

Received: 5 January 2023
Revised: 13 February 2023
Accepted: 24 February 2023
Published: 28 February 2023

1. Introduction

For the past decade, scientists and engineers have made wonderful discoveries about how the addition of a modest quantity of nanoparticles can show a remarkable enhancement in the thermophysical nature of base fluids. The revolutionary idea of adding solid particles to heat exchangers to enhance thermal conductivity was given by Maxwell [1]. The term nanofluids was coined by Choi [2]. Research in multiphase flow has been one of the fields of greater interest since the middle of the 19th century. We can observe this phenomenon in cases ranging from the natural environment to highly evolved industries, i.e., air and water pollution, tornadoes, industrial environments such as the system of combustion and propulsion engines, chemical, biological, food processing, and blood flow inside living organisms, etc. A systematic study on the concept of fluid dynamics of two-phase mixtures was performed by Teletov [3]. Further, Joseph et al. [4] studied immiscible fluids with variable viscosities, where they studied the stability and uniqueness of fluids. Lohrasbi and Sahai [5] conducted a detailed study on the two-phase flow in an infinite channel in the presence of a magnetic field. The authors noticed that electrical and transport properties are time-dependent. Later, Malashetty and Leela [6] analyzed the flow of two immiscible electrically conducting and incompressible fluids with varying thermophysical properties. The authors observed that varying thermophysical properties result in an increment of temperature and velocity. Later, Malashetty et al. [7] extended the same work in vertical closure.

Porous media in heat exchangers are the most used techniques to enhance surface area contact and thermal efficiency. A porous medium is defined as a collection of solid bodies, with adequate open space in or around, which allows fluid to pass through or around them. It has a wide range of applications in absorbing product industries, detergent, textile, foam industries, etc. Vafai and Tien [8] studied the effect of solid boundary and interface forces on the heat transfer properties of the flow saturated with a porous medium. The authors presented a new concept of the momentum boundary layer. The impact of a uniform magnetic field on the flow of two fluids of varying viscosity between two permeable beds was examined by Vajravelu et al. [9]. The author noticed that velocity was optimized in the upper fluid region compared to the lower fluid. Kuznetsov [10] investigated flow between two infinite parallel plates saturated with a rigid wall (porous) by employing the Brinkman–Forchheimer-extended Darcy equation. The author obtained an exact and boundary-layer solution to the problem. In recent developments, Cimpean and Pop [11] examined the flow of nanofluids between infinite plane walls with the angle of inclination γ. The results show that heat transfer enhances the addition of nanoparticles. Similar works were performed by Ahmad and Pop [12]. Chamkha [13] studied the two-layered flow of different fluids, with one channel being porous and the other being non-porous, by incorporating the magnetic field. The author observed that the thermophysical properties of fluids showed improvement with an increase in the ratio of height and thermal conductivity. The flow of Newtonian fluids and micropolar through a porous medium between two rigid boundaries was studied by Yadav et al. [14]. The authors noticed that velocity profile shows enhancement with raise in values of viscosity ratio and couple stress and increasing values of micropolarity parameter decreases velocity.

As technology improves, there is a necessity for heating and cooling in many industries. In these cases, balancing thermal radiation is very important in many industries, such as in the production of glass, designing furnaces, indoor cooling, spacecraft re-entry aerodynamics (operates at high temperature), thermography, combustion process, etc. Similarly, the study of chemical reactions has become more prominent at industry levels. A chemical reaction has its significance in water and food processing, biochemical process, etc. As the fluid flow system is accompanied by an external mass, a chemical reaction takes place. Umavathi et al. [15] analyzed the flow of MHD Poiseuille–Couette between infinite inclined parallel plates maintained at different temperatures. The authors observed that enhancement in temperature and velocity is the result of the dissipation effect and buoyancy forces, respectively. An unsteady flow of a viscous nanofluid through an infinite conduit in the presence of thermal radiation was investigated by Dogonchi and Ganji [16]. The authors noticed that the heat source parameter has a significant effect on the Nusselt number.

Umavathi and Beg [17] investigated the flow of two immiscible fluids in the vertical rectangular duct at the interface. The behavior of water-based copper and copper oxide nanofluids subjected to a magnetic field between two parallel plates was analyzed by Dawar et al. [18]. Aleem et al. [19] looked into the effect of Newtonian heating and species diffusion through a porous vertical plate. The authors noticed that the enhancement of temperature is more in the case of silver nanoparticles with water as a base fluid than in copper nanoparticles. Esmaeilpour and Korzani et al. [20] studied the behavior of the two-phase flow of Newtonian fluid in an inclined channel using the lattice Boltzmann method. The authors observed that an increment in the Hartmann number values enhances the axial velocity of the fluid, which improves the ability of displacement of fluid. Narahari et al. [21] investigated the effect of natural convection on the flow of a nanofluid past a vertical plate. The author noticed that the rise in Brownian motion parameter decreases skin friction while Thermophoresis decreases the Nusselt number. Santhosh et al. [22] conducted a comparative study on dust and nanoparticle in MHD Carreau fluid in a stretching sheet. The study depicts that Boit number and radiation enhance the temperature.

Shah et al. [23] examined two-phase Couette flow in a channel subjected to a magnetic field. Yadav and Kumar [24] conducted a study on the entropy generation of two immiscible fluids in a conduit. The authors concluded that the Hartmann number reduces the linear and micro-rotational velocities. The impact of CNT on the two-phase flow of a nanofluid in an infinite channel was studied by Zeeshan et al. [25]. The study revealed that the volume fraction of nanoparticles has a significant effect on temperature and velocity.

Raju [26] conducted an entropy analysis on the flow of dissipative hybrid nanofluid across a moving flat plate in the presence of thermal radiation and chemical reaction. The author noticed that the rise in the Brinkman number causes entropy to increase while the thermal radiation parameter decreases the temperature. Elmaboud [27] investigated the two-layered flow of conducting and non-conducting fluid in a channel. Hisham et al. [28] examined the flow of two-phase Maxwell fluids between parallel plates. Moreover, and due to the importance of nano/hybrid nanofluids in the enhancement of heat transfer, many researchers have investigated the impact of such fluids along with other physical parameters such as porous media, magnetohydrodynamics, rarefaction effects, and different geometries on the heat transfer [29–41]. The heat and mass transfer in three-layered channels was studied by Umavathi and Hemavathi [42]. Rajeev and Mahantesh investigated heat transfer of nanofluids with non-linear Boussinesq approximation and viscous heating using the differential transform method [43].

Ethylene glycol is widely used in industry as a coolant, antifreeze, heat transfer agent, dehydration of natural gases, etc. Zirconium is a soft, ductile, anticorrosive metal used as components of liquid rocket engines, space, nanowires, nanofibers and catalyst applications, etc. [44]. On the other hand, aluminum oxide nanoparticles are used in pharmaceuticals, materials manufacturing, the mechanical industry, etc. Moreover, the two-phase models are widely used in the flow of oil–water mixtures in pipelines, liquid–liquid solvent extraction mass transfer systems, etc. The relevance of the combined impact of species diffusion and thermal radiation in a two-phase inclined channel received less attention in the research mentioned above. The novelties of the current study are as follows: (i) the significance of thermal radiation and chemical reaction in a two-phase inclined channel through a porous medium, (ii) the analysis of viscous and Darcy dissipation effects, and (iii) the performance of four different nanofluids, namely $EG - Al_2O_3$, $EG - Zr$, $H_2O - Al_2O_3$, and $H_2O - Zr$ on the flow parameters were analyzed. This innovation sets our study apart from earlier studies. The regular perturbation technique was used to determine the solutions of governing equations by analytical method. Hence, a comparison of the enhancement of velocity and temperature in Ethylene glycol and water with different nanoparticles was conducted.

2. Mathematical Formulation

Figure 1 shows the geometrical consideration of clear fluid and nanofluids between two parallel plates with an inclination of angle α. More specifically, the flow under consideration is steady, laminar mixed convective, two-dimensional, incompressible, and fully developed.

The Region I

$(-h \leq y \leq 0)$ is filled up with clear viscous fluid and Region II $(0 \leq y \leq h)$ with nanofluid under the influence of mass diffusion, heat transfer by thermal radiation, and viscous and Darcy dissipation saturated by the porous medium. These infinite plates are kept constant with distinct temperatures and concentrations, i.e., T_{w2}, C_{w2} for the upper plate and T_{w1}, C_{w1} for the lower plate, with $T_{w1} > T_{w2}$ and $C_{w1} > C_{w2}$ respectively [45,46]. The flow is in the x direction. All thermophysical properties for viscous and nanofluids are constant except for density in the buoyancy component of the momentum equation. We consider a constant pressure gradient $\left(-\frac{\partial p}{\partial x}\right)$ using the Oberbeck–Boussinesq approximation. The fluid flow in the channel is driven by pressure and buoyancy forces. Under these assumptions, and employing the Tiwari and Das [47] model for nanofluid, the equations which govern the velocity, temperature, and concentration are given below:

Region I

$$\mu_f \frac{d^2 u_1'}{dy^2} + \rho_f g \beta_f (T_1 - T_{w2}) \cos\alpha + \rho_f g \beta_c (C_1 - C_{w2}) \cos\alpha - \frac{\partial p}{\partial x} = 0 \tag{1}$$

$$k_f \frac{d^2 T_1}{dy'^2} + \mu_f \left(\frac{du'_1}{dy'} \right)^2 - \frac{\partial q_r}{\partial y\prime} = 0 \tag{2}$$

$$D_1 \frac{d^2 C_1}{dy^2} - K_1^* (C_1 - C_{w2}) = 0 \tag{3}$$

Region II

$$\mu_{nf} \frac{d^2 u'_2}{dy'^2} + \left(\rho_{nf} g \beta_{nf} \right) (T_2 - T_{w2}) \cos(\alpha) + \left(\rho_{nf} g \beta_{nc} \right) (C_2 - C_{w2}) \cos(\alpha) - \frac{\mu_{nf}}{K} u'_2 - \frac{\partial p}{\partial x} = 0 \tag{4}$$

$$k_{nf} \frac{d^2 T_2}{dy'^2} + \mu_{nf} \left(\frac{du'_2}{dy'} \right)^2 + \frac{\mu_{nf}}{K} {u'_2}^2 - \frac{\partial q_r}{\partial y\prime} = 0 \tag{5}$$

$$D_2 \frac{d^2 C_2}{dy\prime^2} - K_1^* (C_2 - C_{w2}) = 0 \tag{6}$$

The boundary and interface conditions [45,46,48] are

$$\left. \begin{array}{c} u_1'(y) = 0, T_1(y) = T_{w2}, C_1(y) = C_{w2} \quad at\ y = -h \\ \left. \begin{array}{c} u_1'(y) = u_2'(y), \mu_f \frac{du_1'(y)}{dy'} = \mu_{nf} \frac{du_2'(y)}{dy'} \\ T_1(y) = T_2(y), k_f \frac{dT_1(y)}{dy'} = k_{nf} \frac{dT_2(y)}{dy'} \\ C_1(y) = C_2(y), \frac{dC_1(y)}{dy} = \frac{D_2}{D_1} \frac{dC_2(y)}{dy} \end{array} \right\} at\ y = 0 \\ u_2'(y) = 0, T_2(y) = T_{w1}, C_2(y) = C_{w1} \quad at\ y = h \end{array} \right\} \tag{7}$$

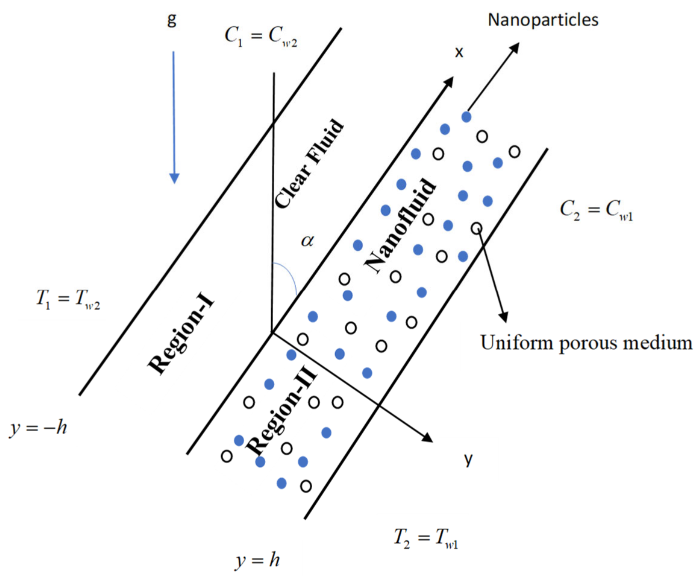

Figure 1. Schematic consideration of the geometric model.

The boundary conditions indicate the no-slip and isothermal conditions at the boundaries. Further, it is assumed that at the interface, there is continuity of velocity, shear stress, temperature, and heat flux.

The effective density, coefficient of thermal expansion, thermal diffusivity, coefficient of solutal expansion, and heat capacitance [49], respectively, are given by

$$\rho_{nf} = (1-\phi)\rho_f + \phi\rho_s \tag{8}$$

$$(\rho\beta)_{nf} = (\rho\beta)_s\phi + (\rho\beta)_f(1-\phi) \tag{9}$$

$$\left(\frac{k_{nf}}{(\rho C_p)_{nf}}\right) = \alpha_{nf} \tag{10}$$

$$(\rho\beta_c)_{nf} = (\rho\beta_c)_s\phi + (\rho\beta_c)_f(1-\phi) \tag{11}$$

$$\left(\rho C_p\right)_{nf} = \left(\rho C_p\right)_f(1-\phi) + \left(\rho C_p\right)_s\phi \tag{12}$$

Effective dynamic viscosity proposed by Brinkman [50,51] is given by

$$\mu_{nf} = \frac{\mu_f}{(1-\phi)^{2.5}} \tag{13}$$

Since the considered nanoparticles are spherical, according to Maxwell [52], the thermal conductivity is given by

$$k_{nf} = k_f\left\{\frac{k_s + 2k_f - 2\phi\left(k_f - k_s\right)}{k_s + 2k_f + \phi\left(k_f - k_s\right)}\right\} \tag{14}$$

Table 1 denotes the thermophysical properties of EG, H_2O, Zr, and Al_2O_3 [53–55].

Table 1. Thermophysical properties of base fluids and nanoparticles.

	ρ (Kg/m^3)	k (W/mk)	β (K^{-1})
H_2O	997.1	0.613	21×10^{-5}
Al_2O_3	3970	40	0.85×10^{-5}
Zr	6506	23	0.0057
EG	1114	0.252	65×10^{-5}

The radiative heat flux [56] term q_r can be obtained by applying the Rosseland approximation [57].

$$q_r = -\frac{4\sigma^*}{3k^*}\frac{\partial}{\partial y\prime}\left(T^4\right) \tag{15}$$

We restrict our study to optically thick fluids by using the Rosseland approximation. Whenever the temperature difference within the flow is small enough, T^4 can be linearized as a combination of temperatures. Expanding to expand T^4 about T_∞, using Taylor's series and neglecting higher order terms, we obtain the following.

$$T^4 = 4T_\infty^3 T - 3T_\infty^4 \tag{16}$$

Equation (15) becomes

$$\frac{\partial q_r}{\partial y\prime} = -\frac{16\sigma^* T_\infty^3}{3k^*}\frac{\partial^2 T}{\partial y\prime^2} \tag{17}$$

Then, (2) and (5) becomes

$$k_f\frac{d^2T_1}{dy'^2} + \mu_f\left(\frac{du_1'}{dy'}\right)^2 + \frac{16\sigma^* T_\infty^3}{3K^*}\frac{d^2T_1}{dy'^2} = 0 \tag{18}$$

$$k_{nf}\frac{d^2T_2}{dy'^2}+\mu_{nf}\left(\frac{du'_2}{dy'}\right)^2+\frac{\mu_{nf}}{K}{u'_2}^2+\frac{16\sigma^*T_\infty^3}{3K^*}\frac{d^2T_2}{dy'^2}=0 \tag{19}$$

Introducing non-dimensional quantities

$$\begin{array}{c} y=\frac{y'}{h},\ u_i=u'_i\left(\frac{\rho_f}{\mu_f}\right)h,\ \theta_i=\frac{T_i-T_{w2}}{T_{w1}-T_{w2}},\ \psi_i=\frac{C_i-C_{w2}}{C_{w1}-C_{w2}}, \\ G_{r1}=\frac{g\beta_f(T_{w1}-T_{w2})h^3}{v_f^2}G_{r2}=\frac{g\beta_c(C_{w1}-C_{w2})h^3}{v_f^2},\ G_{rt}=G_{r1}\mathrm{Cos}(\alpha), \\ G_{rm}=G_{r2}\mathrm{Cos}(\alpha),\ Br=\frac{\mu_f^3}{\rho_f^2h^2(T_{w1}-T_{w2})k_f},\ \sigma=\frac{h}{\sqrt{K}},\ P=-\frac{\rho_fh^3}{\mu_f^2}\frac{\partial p}{\partial x} \\ v_f=\frac{\mu_f}{\rho_f},\ R=\frac{16\sigma^*T_\infty^3}{3K^*k_f},\ Sc=\frac{v}{D},\ Kr=\frac{K_1^*h^2}{\nu_f} \end{array} \tag{20}$$

into (1)–(7) and neglecting dashes (‘), the obtained equations of two regions are as follows:

Region I

$$\frac{d^2u_1}{dy^2}+Grt\theta_1+Grm\psi_1+P=0 \tag{21}$$

$$(1+R)\frac{d^2\theta_1}{dy^2}+Br\left(\frac{du_1}{dy}\right)^2=0 \tag{22}$$

$$\frac{d^2\psi_1}{dy^2}-KrSc_1\psi_1=0 \tag{23}$$

Region II

$$\frac{d^2u_2}{d^2y}+(1-\phi)^{2.5}\left((1-\phi)+\phi\frac{(\rho\beta)_s}{(\rho\beta)_f}\right)Grt\theta_2+(1-\phi)^{2.5}\left((1-\phi)+\phi\frac{(\rho\beta_c)_s}{(\rho\beta_c)_f}\right)Grm\psi_2-\sigma^2u_2+P(1-\phi)^{2.5}=0 \tag{24}$$

$$\left(1+Rc(1-\phi)^{2.5}\right)\frac{d^2\theta_2}{dy^2}+Br\frac{1}{(1-\phi)^{2.5}}\left\{\frac{K_s+2K_f+\phi\left(K_f-K_s\right)}{K_s+2K_f-2\phi\left(K_f-K_s\right)}\right\}\left\{\left(\frac{du_2}{dy}\right)^2+\sigma^2u_2^2\right\}=0 \tag{25}$$

$$\frac{d^2\psi_2}{dy^2}-KrSc_2\psi_2=0 \tag{26}$$

The non-dimensional form of boundary and interface conditions are

$$\left.\begin{array}{c} u_1(y)=0,\theta_1(y)=0,\psi_1(y)=0 \quad at\ y=-1 \\ \left.\begin{array}{r} u_1(y)=u_2(y),\frac{du_1(y)}{dy}=\frac{\mu_{nf}}{\mu_f}\frac{du_2(y)}{dy} \\ \theta_1(y)=\theta_2(y),\frac{d\theta_1(y)}{dy}=\frac{k_{nf}}{k_f}\frac{d\theta_2(y)}{dy} \\ \psi_1(y)=\psi_2(y),\frac{d\psi_1(y)}{dy}=\frac{D_2}{D_1}\frac{d\psi_2(y)}{dy} \end{array}\right\} at\ y=0 \\ u_2(y)=0,\theta_2(y)=1,\psi_2(y)=1aty=1 \quad at\ y=1 \end{array}\right\} \tag{27}$$

3. Solution Method

To solve Equations (21)–(26), the regular perturbation technique is employed, due to the coupled and non-linear nature of equations. Using the Brinkman number as a perturbation parameter, the following are the approximate solutions for velocity, temperature, and concentration:

$$\left.\begin{array}{c} u_i=u_{i0}+Bru_{i1}+Br^2u_{i2}+\ldots \\ \theta_i=\theta_{i0}+Br\theta_{i1}+Br^2\theta_{i2}+\ldots \\ \psi_i=\psi_{i0}+Br\psi_{i1}+Br^2\psi_{i2}+\ldots \end{array}\right\} \tag{28}$$

where u_i, θ_i and ψ_i are the functions of variable y.

Substituting (28) into (21)–(27), we obtain the equations for zeroth and first-order equations, together with the corresponding boundary and interface conditions which are obtained by equating like powers of Br and ignoring Br^2 and higher-order terms.

Zeroth order equations

Region I:

$$\frac{d^2u_{10}}{dy^2} + Grt\theta_{10} + Grm\psi_{10} + P = 0 \tag{29}$$

$$\frac{d^2\theta_{10}}{dy^2} = 0 \tag{30}$$

$$\frac{d^2\psi_{10}}{dy^2} - KrSc_1\psi_{10} = 0 \tag{31}$$

Region II:

$$\frac{d^2u_{20}}{d^2y} + (1-\phi)^{2.5}\left((1-\phi) + \phi\frac{(\rho\beta)_s}{(\rho\beta)_f}\right)G_{rt}\theta_{20} + (1-\phi)^{2.5}\left((1-\phi) + \phi\frac{(\rho\beta_c)_s}{(\rho\beta_c)_f}\right)G_{rm}\psi_{20} - \sigma^2u_{20} + P(1-\phi)^{2.5} = 0 \tag{32}$$

$$\frac{d^2\theta_{20}}{dy^2} = 0 \tag{33}$$

$$\frac{d^2\psi_{20}}{dy^2} - KrSc_2\psi_{20} = 0 \tag{34}$$

The corresponding boundary and interface conditions are

$$\left.\begin{array}{c} u_{10}(-1) = 0,\ u_{10}(0) = u_{20}(0),\ \ \frac{du_{10}}{dy}(0) = \frac{\mu_{nf}}{\mu_f}\frac{du_{20}}{dy}(0),\ \ u_{20}(1) = 0 \\ \theta_{10}(-1) = 0,\ \ \theta_{10}(0) = \theta_{20}(0), \frac{d\theta_{10}}{dy}(0) = \frac{k_{nf}}{k_f}\frac{d\theta_{20}}{dy}(0),\ \theta_{20}(1) = 1 \\ \psi_{10}(-1) = 0,\ \ \ \psi_{10}(0) = \psi_{20}(0),\ \ \frac{d\psi_{10}}{dy}(0) = \frac{D_2}{D_1}\frac{d\psi_{20}}{dy}(0),\ \ \psi_{20}(1) = 1 \end{array}\right\} \tag{35}$$

First-order Equations

Region I:

$$\frac{d^2u_{11}}{dy^2} + Grt\theta_{11} + Grm\psi_{11} = 0 \tag{36}$$

$$(1+R)\frac{d^2\theta_{11}}{dy^2} + \left(\frac{du_{10}}{dy}\right)^2 = 0 \tag{37}$$

$$\frac{d^2\psi_{11}}{dy^2} - KrSc_1\psi_{11} = 0 \tag{38}$$

Region II:

$$\frac{d^2u_{21}}{d^2y} + (1-\phi)^{2.5}\left((1-\phi) + \phi\frac{(\rho\beta)_s}{(\rho\beta)_f}\right)Grt\theta_{21} + (1-\phi)^{2.5}\left((1-\phi) + \phi\frac{(\rho\beta_c)_s}{(\rho\beta_c)_f}\right)Grm\psi_{21} - \sigma^2u_{21} = 0 \tag{39}$$

$$\left(1 + Rc(1-\phi)^{2.5}\right)\frac{d^2\theta_{21}}{dy^2} + \frac{1}{(1-\phi)^{2.5}}\left\{\frac{K_s + 2K_f + \phi\left(K_f - K_s\right)}{K_s + 2K_f - 2\phi\left(K_f - K_s\right)}\right\}\left\{\left(\frac{du_{20}}{dy}\right)^2 + \sigma^2u_{20}^2\right\} = 0 \tag{40}$$

$$\frac{d^2\psi_{21}}{dy^2} - KrSc_2\psi_{21} = 0 \tag{41}$$

The corresponding boundary and interface conditions are

$$\left.\begin{array}{c} u_{11}(-1)=0,\ u_{11}(0)=u_{21}(0),\ \frac{du_{11}}{dy}(0)=\frac{\mu_{nf}}{\mu_f}\frac{du_{21}}{dy}(0),\ u_{21}(1)=0 \\ \theta_{11}(-1)=0,\ \theta_{11}(0)=\theta_{21}(0), \frac{d\theta_{11}}{dy}(0)=\frac{k_{nf}}{k_f}\frac{d\theta_{21}}{dy}(0),\ \theta_{21}(1)=0 \\ \psi_{11}(-1)=0,\ \ \psi_{11}(0)=\psi_{21}(0),\ \frac{d\psi_{11}}{dy}(0)=\frac{D_2}{D_1}\frac{d\psi_{21}}{dy}(0),\ \psi_{21}(1)=0 \end{array}\right\} \tag{42}$$

Below are the solutions to zeroth and first-order equations using boundary and interface conditions.

Concentration distribution:

$$\psi_{10}=c_5\mathrm{Cosh}\sqrt{N_3}y+c_6\mathrm{Sinh}\sqrt{N_3}y \tag{43}$$

$$\psi_{20}=c_7\mathrm{Cosh}\sqrt{N_4}y+c_8\mathrm{Sinh}\sqrt{N_4}y \tag{44}$$

Temperature distribution:

$$\theta_{10}=c_1y+c_2 \tag{45}$$

$$\theta_{20}=c_3y+c_4 \tag{46}$$

$$\begin{array}{c}\theta_{11}=-\frac{1}{N_1}\left[L_{16}y^6+L_{17}y^5+L_{18}y^4+L_{19}y^3+\frac{b_{11}^2}{2}y^2+L_{20}\cosh\left(2y\sqrt{N_3}\right)+L_{21}\sinh\left(2y\sqrt{N_3}\right)\right. \\ +L_{22}\cosh\left(y\sqrt{N_3}\right)+L_{23}\sinh\left(y\sqrt{N_3}\right)+L_{24}y\cosh\left(y\sqrt{N_3}\right)+L_{25}y\sinh\left(y\sqrt{N_3}\right) \\ \left.+L_{26}\sinh\left(y\sqrt{N_3}\right)\left(2+y^2N_3\right)+L_{27}\cosh\left(y\sqrt{N_3}\right)\left(2+y^2N_3\right)\right]+b_{31}y+b_{32}\end{array} \tag{47}$$

$$\begin{array}{c}\theta_{21}=-\frac{c}{N_2}\left[L_{41}\cos h\left(2y\sqrt{N_4}\right)+L_{43}\sin h2\sigma y+L_{44}cosh2\sigma y+L_{45}\sin h2\sqrt{N_4}y+L_{46}\sin h\left(\sqrt{N_4}y\right)\cos h(\sigma y)\right. \\ +L_{47}\sin h\left(\sqrt{N_4}y\right)\sin h(\sigma y)+L_{48}\cos h\left(\sqrt{N_4}y\right)\cos h(\sigma y)+L_{49}\sin h(\sigma y)\cos h\left(\sqrt{N_4}y\right) \\ +L_{50}\cos h(y\sigma)+L_{51}cosh\left(\sqrt{N_4}y\right)+L_{52}\sin h\left(y\sqrt{N_4}\right)+L_{53}\sin h\sigma y+L_{54}y\cos h(y\sigma) \\ \left.+L_{55}y\sin h\left(y\sqrt{N_4}\right)+L_{56}y\cos h\left(y\sqrt{N_4}\right)+L_{57}y\sin h(y\sigma)+L_{58}y^4+L_{59}y^3+(L_{60}+L_{42})y^2\right]+b_{41}y+b_{42}\end{array} \tag{48}$$

Velocity:

$$u_{10}=\frac{L_1}{N_3}\cosh\sqrt{N_3}y+\frac{L_2}{N_3}\sinh\sqrt{N_3}y+\frac{L_3}{6}y^3+\frac{L4}{2}y^2+b_{11}y+b_{12} \tag{49}$$

$$u_{20}=b_{21}\mathrm{Cosh}\sigma y+b_{22}\mathrm{Sinh}\sigma y+\frac{L_5}{(N_4-\sigma^2)}\mathrm{Cosh}\sqrt{N_4}y+\frac{L_6}{(N_4-\sigma^2)}\mathrm{Sinh}\sqrt{N_4}y-\frac{(L_7y+L_8)}{\sigma^2} \tag{50}$$

$$\begin{array}{c}u_{11}=\frac{G_{rt}}{N_1}\left[L_{28}y^8+L_{29}y^7+L_{30}y^6+L_{31}y^5+L_{32}y^4+L_{33}\cos\mathrm{h}\left(2y\sqrt{N_3}\right)+L_{34}\sin\mathrm{h}\left(2y\sqrt{N_3}\right)\right. \\ +L_{35}\cos\mathrm{h}\left(y\sqrt{N_3}\right)+L_{36}\sin\mathrm{h}\left(y\sqrt{N_3}\right)+L_{37}y\cos\mathrm{h}\left(y\sqrt{N_3}\right)+L_{38}y\sin\mathrm{h}\left(y\sqrt{N_3}\right) \\ \left.+L_{26}y^2\sin\mathrm{h}\left(y\sqrt{N_3}\right)+L_{27}y^2\cos\mathrm{h}\left(y\sqrt{N_3}\right)\right]-G_{rt}\left(\frac{b_{31}}{6}y^3+\frac{b_{32}}{2}y^2\right) \\ -G_{rm}\left(\frac{c_9}{N_3}\cos\mathrm{h}\sqrt{N_3}y+\frac{c_{10}}{N_3}\sin\mathrm{h}\sqrt{N_3}y\right)+b_{51}y+b_{52}\end{array} \tag{51}$$

$$\begin{array}{l}u_{21}=b_{61}\cos\mathrm{h}\sigma y+b_{62}\sin\mathrm{h}\sigma y \\ +\frac{aG_{rt}c}{N_2}\left[L_{61}\cos\mathrm{h}\left(2y\sqrt{N_4}\right)+L_{62}\mathrm{Sinh}2\sigma y+L_{63}\mathrm{Cosh}2\sigma y+L_{64}\mathrm{Sinh}2\sqrt{N_4}y+L_{65}\sin\mathrm{h}\left(\sigma+\sqrt{N_4}\right)y\right. \\ +L_{66}\sin\mathrm{h}\left(\sigma-\sqrt{N_4}\right)y+L_{67}\cos\mathrm{h}\left(\sigma+\sqrt{N_4}\right)y+L_{68}\cos\mathrm{h}(\sigma-N_4)y+L_{69}y\sin\mathrm{h}\sigma y \\ +L_{70}\mathrm{Cosh}\sqrt{N_4}y+L_{71}\sin\mathrm{h}y\sqrt{N_4}+L_{72}y\cos\mathrm{h}\sigma y+\frac{L_{54}}{4\sigma}y^2\sin\mathrm{h}\sigma y+\frac{L_{55}}{4\sqrt{N_4}}y^2\cos\mathrm{h}\sqrt{N_4}y \\ -\frac{L_{55}}{4N_4}y\sin\mathrm{h}\sqrt{N_4}y+\frac{L_{56}}{4\sqrt{N_4}}y^2\sin\mathrm{h}\sqrt{N_4}y-\frac{L_{56}}{4N_4}y\cos\mathrm{h}\sqrt{N_4}y+\frac{L_{57}}{4\sigma}y^2\cos\mathrm{h}\sigma y \\ \left.-\frac{1}{\sigma^2}\left(L_{58}y^4+L_{59}y^3+(L_{60}+L_{42})y^2+\frac{(12L_{58}y^2+6L_{59}y+2(L_{60}+L_{42}))}{\sigma^2}+\frac{(24L_{58})}{\sigma^4}\right)\right] \\ +\frac{aG_{rt}}{\sigma^2}(b_{41}y+b_{42})-\frac{bG_{rm}}{(N_4-\sigma^2)}\left(c_{11}\mathrm{Cosh}\sqrt{N_4}y+c_{12}\mathrm{Sinh}\sqrt{N_4}y\right)\end{array} \tag{52}$$

where $c_1, c_2 \ldots c_{12}, d_1, d_2, d_3, K_1, K_2, \ldots K_{12}$, and $L_1, L_2, \ldots L_{72}$ are constants.

Therefore, the solution of clear fluid and nanofluid region are

$$\left.\begin{array}{l}\psi_1 = \psi_{10}\\ \psi_2 = \psi_{20}\end{array}\right\} \tag{53}$$

$$\left.\begin{array}{l}\theta_1 = \theta_{10} + Br\theta_{11}\\ \theta_2 = \theta_{20} + Br\theta_{21}\end{array}\right\} \tag{54}$$

$$\left.\begin{array}{l}u_1 = u_{10} + Bru_{11}\\ u_2 = u_{20} + Bru_{21}\end{array}\right\} \tag{55}$$

where ψ_i, θ_i and u_i $(i = 0, 1, 2)$ are functions of y.

With regard to the rate of heat transfer and shear stress, the Nusselt number (Nu) and skin friction coefficient (Sk) at the surfaces in the non-dimensional form are as follows:

Nusselt number: $(Nu_1) = \left(\frac{d\theta_1}{dy}\right)$ at $y = -1$, $(Nu_2) = \left(\frac{d\theta_2}{dy}\right)$ at $y = 1$

Skin friction coefficient: $(Sk_1) = \left(\frac{du_1}{dy}\right)$ at $y = -1$, $(Sk_2) = -\left(\frac{du_2}{dy}\right)$ at $y = 1$

4. Results and Discussion

A two-layered flow of viscous and water/ethylene glycol-based nanofluids between parallel plates with the angle of inclination α in the presence of mass diffusion and thermal radiation was analyzed. The perturbation technique is used to solve the problem by considering Br as a parameter to obtain velocity, temperature, and concentration profiles. The Nusslet number and skin friction coefficient are calculated. The behavior of velocity, temperature, and concentration is examined by varying the Thermal Grashof number $(1 \leq G_{rt} \leq 15)$, solute Grashof Number $(1 \leq G_{rm} \leq 15)$, solid volume fraction $(0.01 \leq \phi \leq 0.05)$, porous parameter $(2 \leq \sigma \leq 8)$, chemical reaction parameter Kr, and Schmidt number $Sc(Sc_1 = Sc_2)$, and radiation parameter R is investigated for different nanoparticles and base fluids. In this study, we considered aluminum oxide (Al_2O_3) and zirconium (Zr) as nanoparticles with ethylene glycol (EG) and water (H_2O) as base fluids.

For the graphs and tables, we assumed the following as fixed. Namely,

$$\alpha = \pi/4, G_{rt} = 5, G_{rm} = 5, \sigma = 4, Br = 0.5, P = 5, R = 1.8, Sc = 0.6(H_2O), Sc = 1.5(EG), Kr = 0.9, \frac{D_2}{D_1} = 1, \phi = 0.02$$

Figure 2 depicts the influence of the Schmidt number on the concentration field in the presence of Al_2O_3 nanoparticles and water as a base fluid. It is clear that the concentration subsides as the Schmidt number increases. On choosing Sc values for hydrogen, helium, water vapor, and ammonia, the concentration profile subsides. The Schmidt number increases as the solute diffusivity decreases, permitting shallower penetration of the solute effect. Due to this, concentration decreases as Sc increases.

Figure 3 shows the impact of the Kr on the concentration field. Here, the graph is drawn by considering Al_2O_3 with EG as the first case and Al_2O_3 with H_2O as the second case. In both cases, concentration diminishes with increasing values of Kr. Specifically, $Kr > 0$ corresponds to destructive chemical reactions and $Kr < 0$ corresponds to generative chemical reactions. As the chemical reaction parameter increases, the number of solute molecules undergoing chemical reactions increases, resulting in a decrease in the concentration field. Similar effects are observed by Kataria and Patel [58] and Chamka [59].

The influence of G_{rm} on temperature and velocity profiles are illustrated in Figures 4 and 5. Here, a comparison is made between different nanoparticles and base fluids, as mentioned above. When Region I is filled with EG, and Region II is occupied with $EG - Al_2O_3$ nanofluid through a porous medium, Figure 4 demonstrates that increasing the G_{rm} increases the temperature in both areas. That means temperature initially increases in Region I and acquires parabolic behavior with temperature enhancement in Region II. Since the G_{rm} is the ratio of buoyancy forces (species) to viscous force, a rise in the value of G_{rm} strengthens the species buoyancy force resulting in a rise in the temperature and velocity of the fluid. It is seen from the graph that EG with Zr, H_2O with Al_2O_3, and H_2O with Zr show the same behavior. However, enhancement of temperature is comparatively high in H_2O with Zr. Figure 5 displays the impact G_{rm} on velocity profiles. When EG is used as the base fluid, a good enhancement of velocity is noticed in the clear fluid region than in the nanofluid region in the case of Al_2O_3 nanoparticles. While for EG with Zr nanofluids, both in Region I and Region II, the velocity is distributed equally. In the case of water as a base fluid, enhancement of velocity is high in Region I for Al_2O_3 and behaves completely differently in the case of $H_2O - Zr$. That is, in the clear fluid region, the velocity first increases, and at the interface, it exhibits a minor increase before becoming constant at a specific point in Region II, and then an opposite phenomenon is observed, particularly in the case of $H_2O - Zr$.

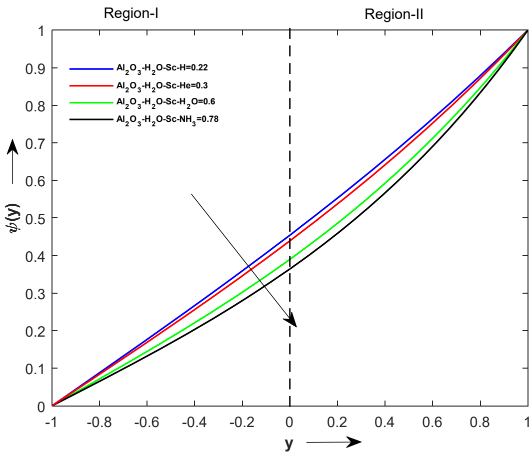

Figure 2. Effect of Sc on Concentration where $\phi = 0.02$, $Grt = 5, Grm = 5,\ \sigma = 4, Br = 0.5, P = 5$, R = 1.8, $Kr = 0.9$.

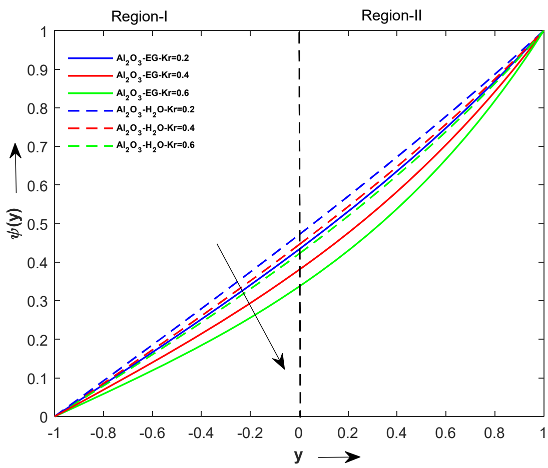

Figure 3. Impact of Kr on concentration where $\phi = 0.02, Grt = 5, Grm = 5, \sigma = 4, Br = 0.5$, P = 5, $R = 1.8, Sc_{(H_2O)} = 0.6, Sc_{(EG)} = 1.5$.

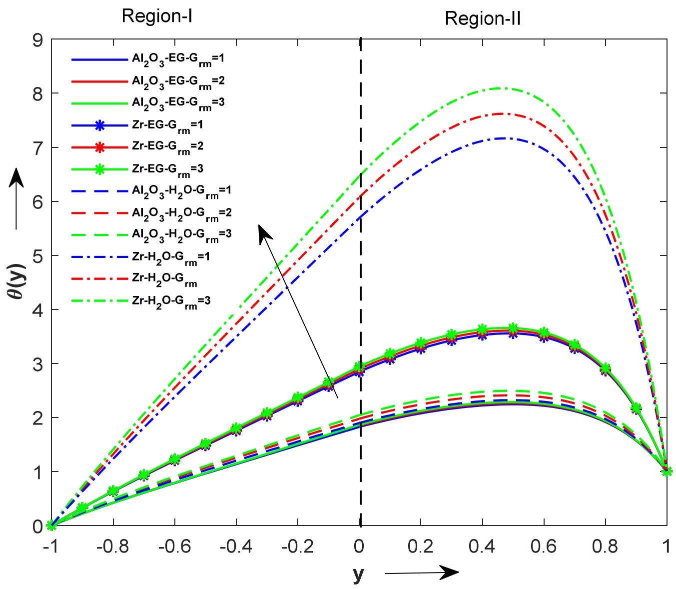

Figure 4. Impact of G_{rm} on temperature where $\phi = 0.02$, $G_{rt} = 5, \sigma = 4, Br = 0.5, R = 1.8, Sc_{(H_2O)} = 0.6, Sc_{(EG)} = 1.5,\ \ Kr = 0.9,\ \alpha = \pi/4$.

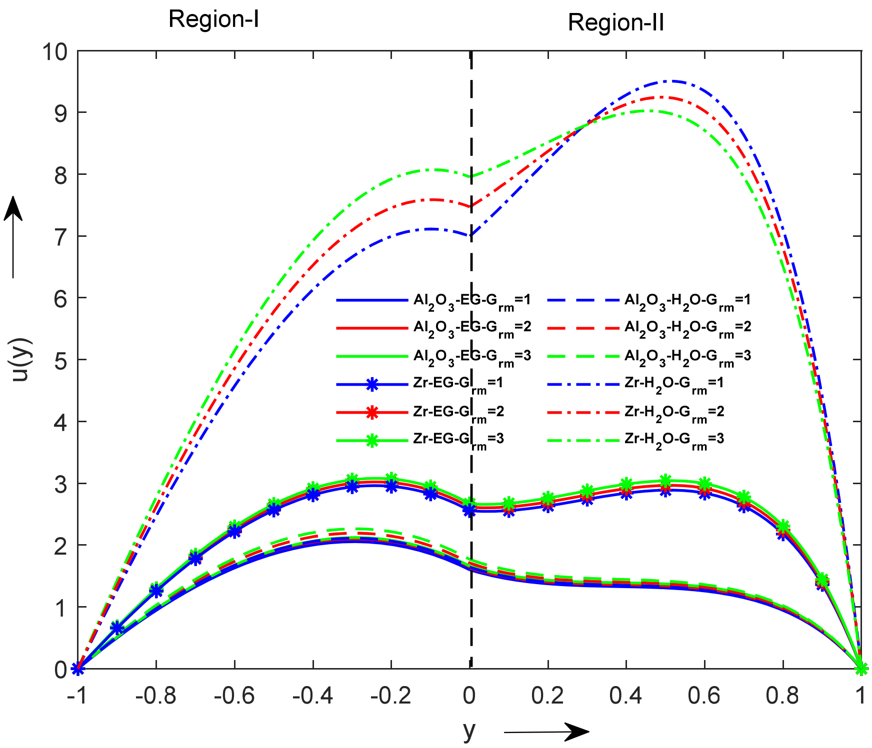

Figure 5. Impact of G_{rm} on velocity where $\phi = 0.02$, $G_{rt} = 5, \sigma = 4, Br = 0.5, R = 1.8, Sc_{(H_2O)} = 0.6, Sc_{(EG)} = 1.5,\ \ Kr = 0.9,\ \alpha = \pi/4$.

Furthermore, Figures 6 and 7 show the temperature and velocity profiles for varying values of G_{rt} for Al_2O_3 and Zr with EG and H_2O as base fluids. Convection causes the buoyancy forces due to the temperature gradient. So, as G_{rt} increases, the buoyancy forces dominate the flow and result in the enhancement of the temperature and velocity of the fluid. For increasing values of G_{rt}, the temperature increases in the clear fluid region and enhancement of temperature can be noticed in the nanofluid region in all the cases. More specifically, when EG is the base fluid, Zr shows a maximum increment of temperature higher than Al_2O_3. The $H_2O - Zr$ nanofluid exhibit more temperature enhancement.

Additionally, velocity initially increases in the clear fluid region while decreasing in Region II, which is saturated with a porous medium in all the cases. Here, also optimal velocity is observed in H_2O with Zr nanoparticles in the clear fluid region. These results are identical to Kumar et al. [45] in the absence of nanofluids.

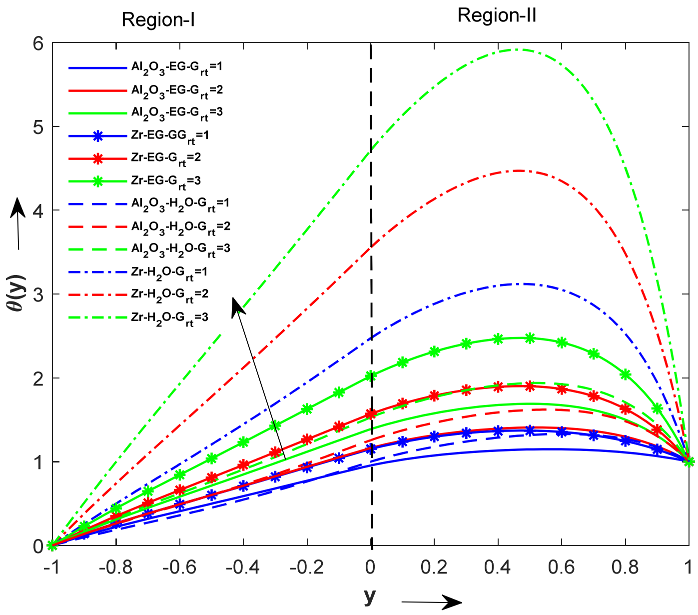

Figure 6. Impact of G_{rt} on temperature where $\phi = 0.02$, $G_{rm} = 5, \sigma = 4, Br = 0.5, R = 1.8, Sc_{(H_2O)} = 0.6, Sc_{(EG)} = 1.5,\ \ Kr = 0.9,\ \alpha = \pi/4$.

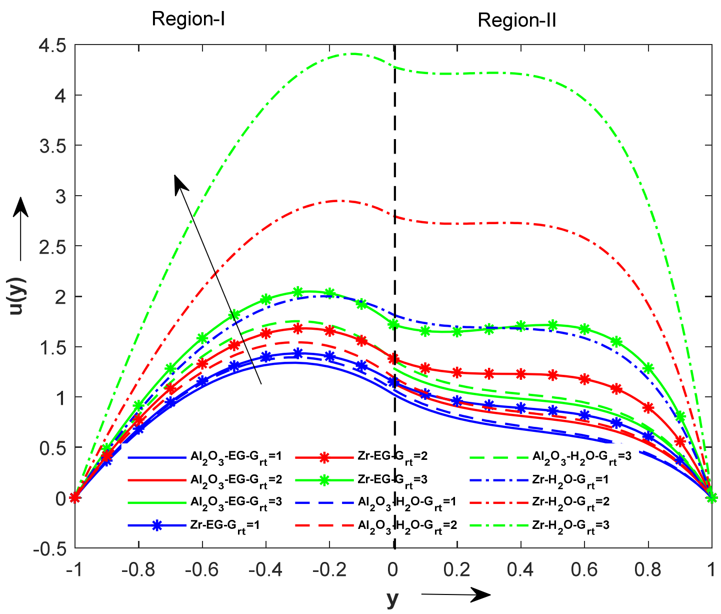

Figure 7. Impact of G_{rt} on velocity where $\phi = 0.02$, $G_{rm} = 5, \sigma = 4, Br = 0.5, R = 1.8, Sc_{(H_2O)} = 0.6, Sc_{(EG)} = 1.5,\ \ Kr = 0.9,\ \alpha = \pi/4$.

Figures 8 and 9 illustrate the graphical representation of temperature and velocity distributions for various base fluids and nanoparticles. Physical interpretation of Br is the ratio of heat by viscous dissipation to molecular conduction. Fluid temperature increases as a result of the increased internal resistance of nanoparticles within the fluid, as shown in Figure 6. In comparison to EG and water, the enhancement of temperature is maximum when Zr nanoparticles are added to water. Additionally, the next maximum enhancement is observed for EG with Zr than Al_2O_3. Figure 9 shows the impact of Br on velocity. As Br increases, both regions experience an increase in velocity. Moreover, velocity increment is more prevalent in the clear fluid region than in the nanofluid region (saturated with porous medium). Here, the behavior of nanoparticles and base fluids remains the same as the temperature.

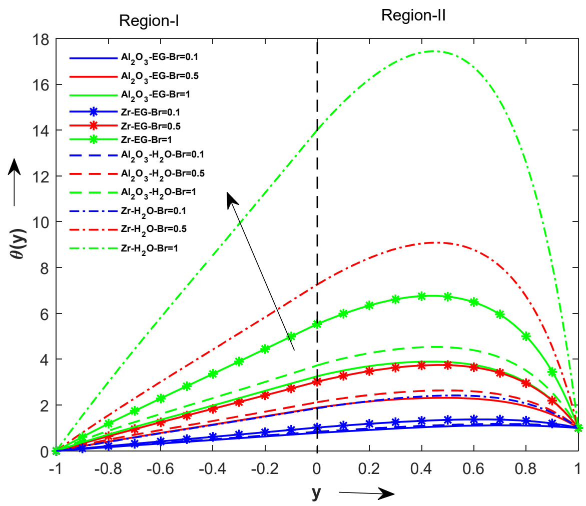

Figure 8. Impact of Br on temperature where $\phi = 0.02, G_{rt} = 5, G_{rm} = 5,\ \sigma = 4, R = 1.8, Sc_{(H_2O)} = 0.6, Sc_{(EG)} = 1.5,\ \ Kr = 0.9,\ \alpha = \pi/4$.

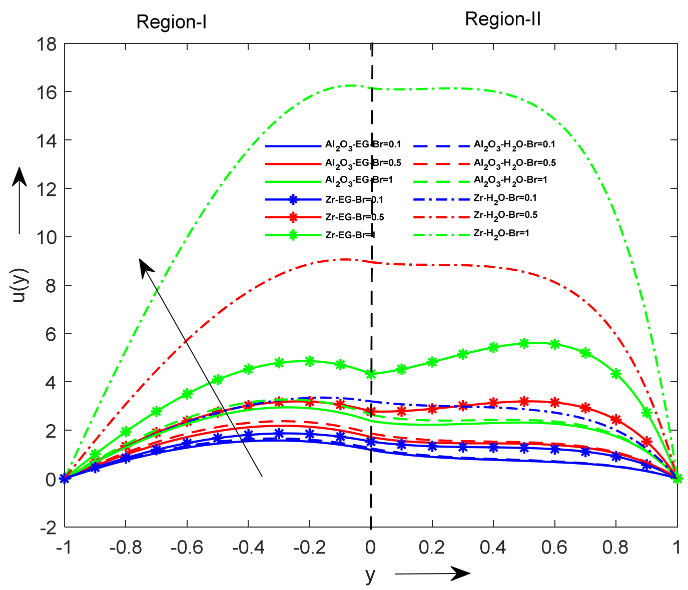

Figure 9. Impact of Br on velocity where $\phi = 0.02, G_{rt} = 5, G_{rm} = 5,\ \sigma = 4, R = 1.8, Sc_{(H_2O)} = 0.6, Sc_{(EG)} = 1.5,\ \ Kr = 0.9,\ \alpha = \pi/4$.

The impact of inclination α on temperature and velocity are shown in Figures 10 and 11, respectively. In all cases, the temperature and velocity of the fluid decrease with an increase in α due to the pressure exerted on it. In Figure 8, the decreasing temperature profile is observed for all nanofluids. However, enhancement is high in the nanofluid region for Zr with water. Furthermore, Figure 11 shows decreasing velocity profile in all the cases for increasing values of α. However, in the case of H_2O with Zr, the increment of velocity is notably higher in Region I than in the nanofluid region. The enhancement of velocity is greater in the nanofluid region in the presence of EG with Zr.

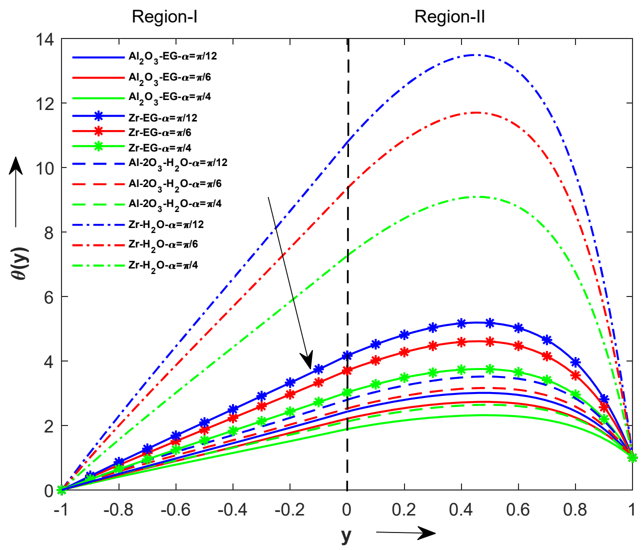

Figure 10. Impact of α on temperature, $G_{rt} = 5, G_{rm} = 5,\ \sigma = 4, Br = 0.5, R = 1.8, Sc_{(H_2O)} = 0.6, Sc_{(EG)} = 1.5,\ \ Kr = 0.9$.

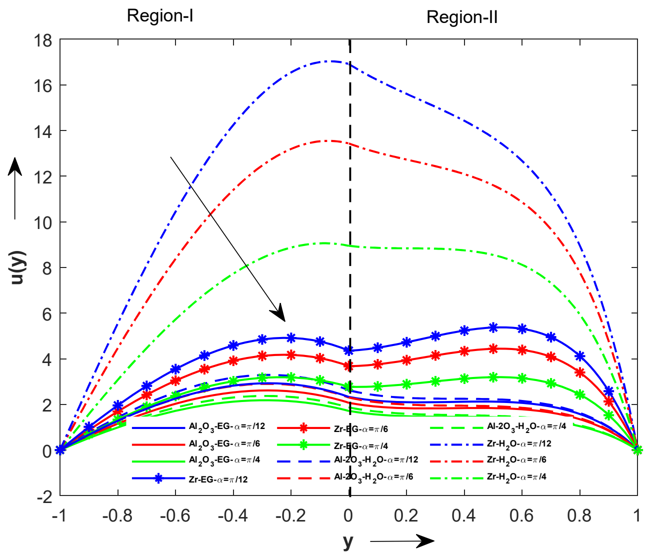

Figure 11. Impact of α on velocity $\phi = 0.02$, $G_{rt} = 5, G_{rm} = 5,\ \sigma = 4, Br = 0.5, R = 1.8, Sc_{(H_2O)} = 0.6, Sc_{(EG)} = 1.5,\ \ Kr = 0.9$.

Figures 12 and 13 reveal the impact of ϕ on temperature and velocity, respectively. The concentration of a particular phase is governed by solid volume fraction. A higher volume fraction results in a more intense temperature profile. The escalating volume fraction of nanoparticles greatly enhances the fluid's thermal conductivity, resulting in an increase in temperature. This outcome is well in line with Mahantesh et al. [49]. However, velocity profiles show the opposite phenomenon, which can be depicted in Figure 13.

Figure 14 outlines the impact of the R on temperature. The thermal efficiency of the fluid diminishes as R increases. The influence of radiation reduces the action of convection by considerably lowering the temperature difference between the fluid and the channel walls, causing the temperature to fall. Figures 15 and 16 demonstrate the impact of the σ on temperature and velocity. Figure 15 exemplifies that the temperature rises with the rise in the porosity parameter. The flow is generally impeded by the porous medium. However, flow through porous media generates friction, which leads to an increase in thermal conductivity and a rise in temperature. The optimal enhancement of temperature is observed for Zr nanoparticles with water as a base fluid in Region II, while EG with Al_2O_3 shows the least enhancement of temperature.

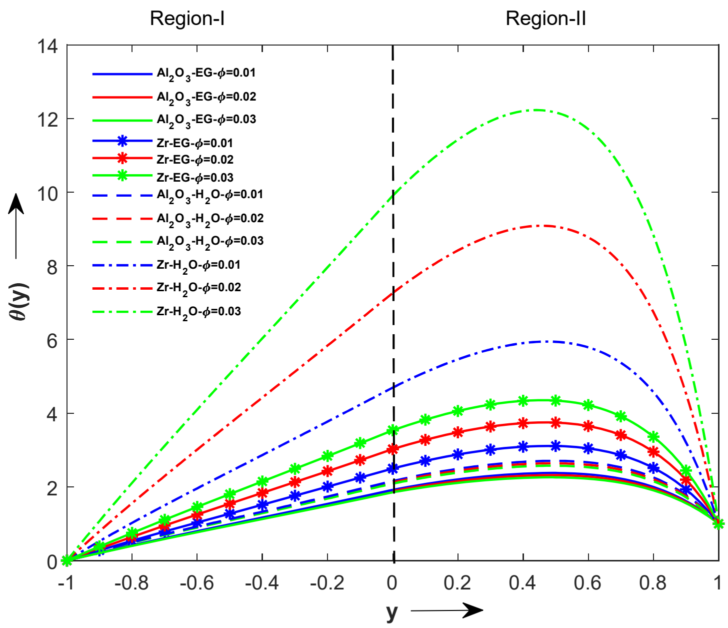

Figure 12. Impact of ϕ on temperature where $\alpha = \pi/4$, $Grt = 5, Grm = 5,\ \sigma = 4, Br = 0.5, R = 1.8, Sc_{(H_2O)} = 0.6, Sc_{(EG)} = 1.5,\ \ Kr = 0.9$.

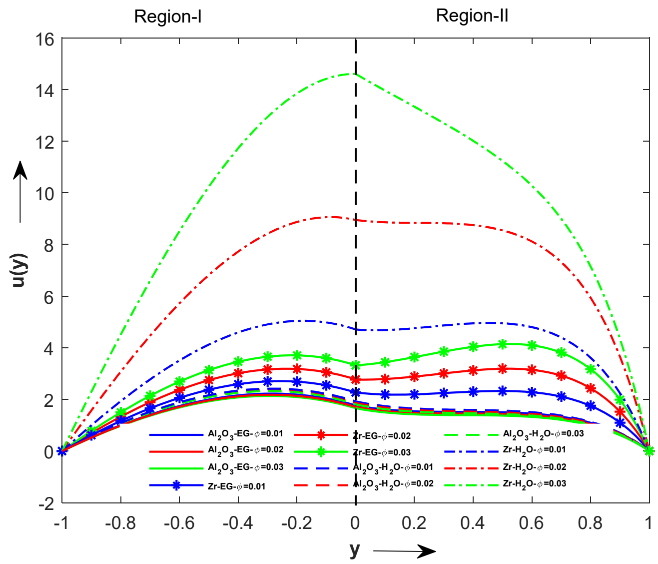

Figure 13. Impact of ϕ on velocity where $\alpha = \pi/4$, $Grt = 5, Grm = 5,\ \sigma = 4, Br = 0.5, R = 1.8, Sc_{(H_2O)} = 0.6, Sc_{(EG)} = 1.5,\ \ Kr = 0.9$.

On the other hand, Figure 16 shows the velocity profile of Al_2O_3 with water and EG. Both regions experience a drop in velocity when the porosity parameter is increased. However, velocity is predominantly less in Region II, as it consists of a nanofluid with a porous medium. However, the enhancement temperature is high for water in the clear fluid region. Physically, the porous medium is an obstruction to the flow. Hence, as the porosity parameter increases, the velocity decreases.

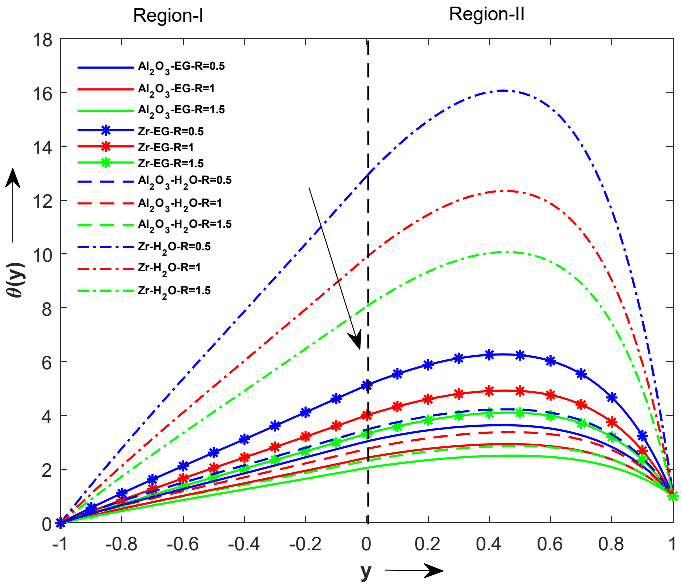

Figure 14. Impact of R on temperature where $\phi = 0.02$, $G_{rt} = 5, G_{rm} = 5$, $\sigma = 4, Br = 0.5, \alpha = \pi/4, Sc_{(H_2O)} = 0.6, Sc_{(EG)} = 1.5$, $Kr = 0.9$.

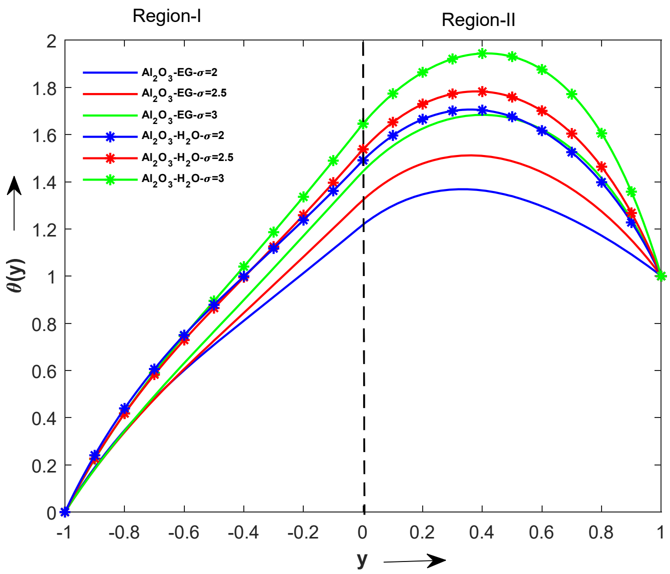

Figure 15. Impact of σ on temperature where $\phi = 0.02$, $G_{rt} = 5, G_{rm} = 5$, $\sigma = 4, Br = 0.5, \alpha = \pi/4, Sc_{(H_2O)} = 0.6, Sc_{(EG)} = 1.5$, $Kr = 0.9$.

The Nusselt number and skin friction coefficient are significant from an engineering point of view. Figure 17 shows the variation of Nusselt number at the upper plate with increasing values of G_{rt} and G_{rm} for a different combination of base fluids and nanoparticles. Figure 17a,b denote the impact of G_{rt} and G_{rm} on Nusselt number for EG and H_2O-based nanofluids. In particular, it is depicted that Zr nanoparticles boost the rate of heat transfer in both the base fluids, which is comparatively high when water is a base fluid. Because G_{rt} and G_{rm} represent the buoyancy forces caused by variations in the fluid density, the increase in their values lowers the viscous forces. So, the Nusselt number increases. Similarly, by treating G_{rt} as constant, we can examine the impact of G_{rm} on the Nusselt number. Hence, buoyancy forces enhance the convection, resulting in the maximum heat transfer rate.

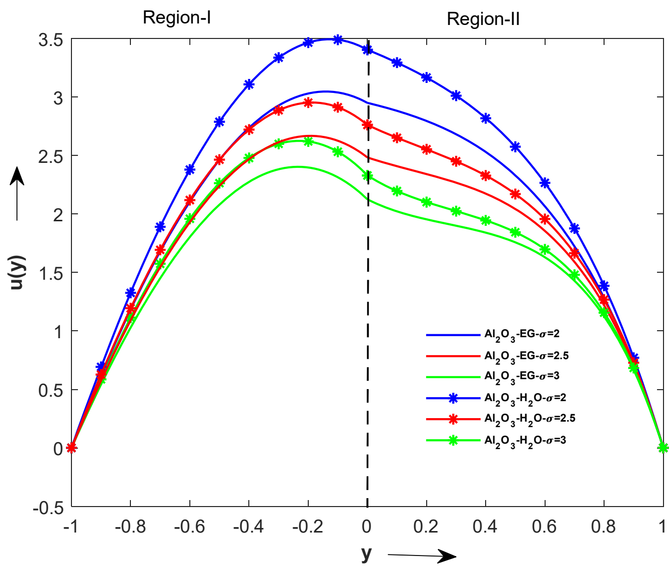

Figure 16. Impact of σ on velocity.

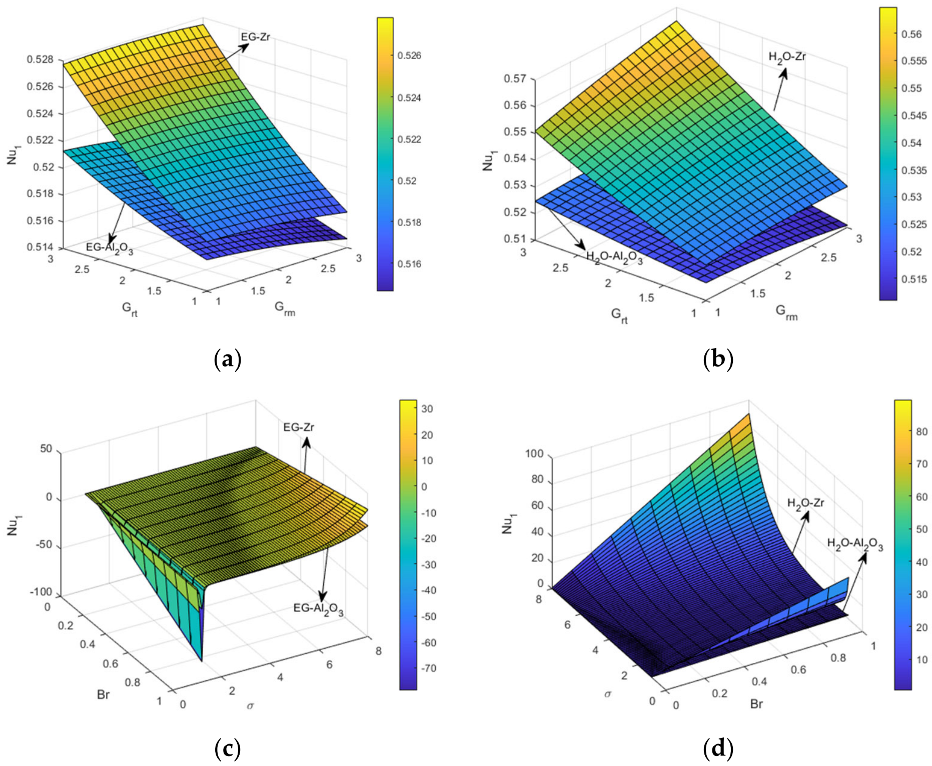

Figure 17. The variation in Nusselt number at upper plate (**a**) G_{rt} and G_{rm} for EG, (**b**) G_{rt} and G_{rm} for H_2O, (**c**) Br and σ for EG, (**d**) Br and σ for H_2O.

The effects of Br and σ for EG- and H_2O-based nanofluids at the upper plate are depicted in Figure 17c,d. In Figure 17c, the $EG - Zr$ nanofluid outperforms Al_2O_3 nanoparticles in terms of heat transfer rate as the Br value rises. Although we obtain better heat transfer from the $H_2O - Zr$ nanofluid. Br has the highest rate of heat transfer when compared to other parameters, because an increase in Br causes conduction from the wall to the fluid. Additionally, increasing σ initially enhances the rate of heat transfer, but as σ rises, the rate sharply declines. Figure 18a,b demonstrate the effects of G_{rt} and G_{rm} on the Nusselt number at the lower plate. The $H_2O - Zr$ nanoparticle exhibits the highest rate of heat transfer. Additionally, color profiles show that the lower plate transfers heat at a quicker rate. Moreover, Figure 18c,d resemble the impacts of Br and σ. The Nusselt number increases for $EG - Al_2O_3$ nanofluids and decreases for $EG - Zr$ nanofluids as a result of rising Br and σ values. However, for H_2O-based nanofluids, the rate of heat transfer is relatively high. The Nusselt number significantly drops for high values of the porosity parameter, as indicated by the graph's color transition.

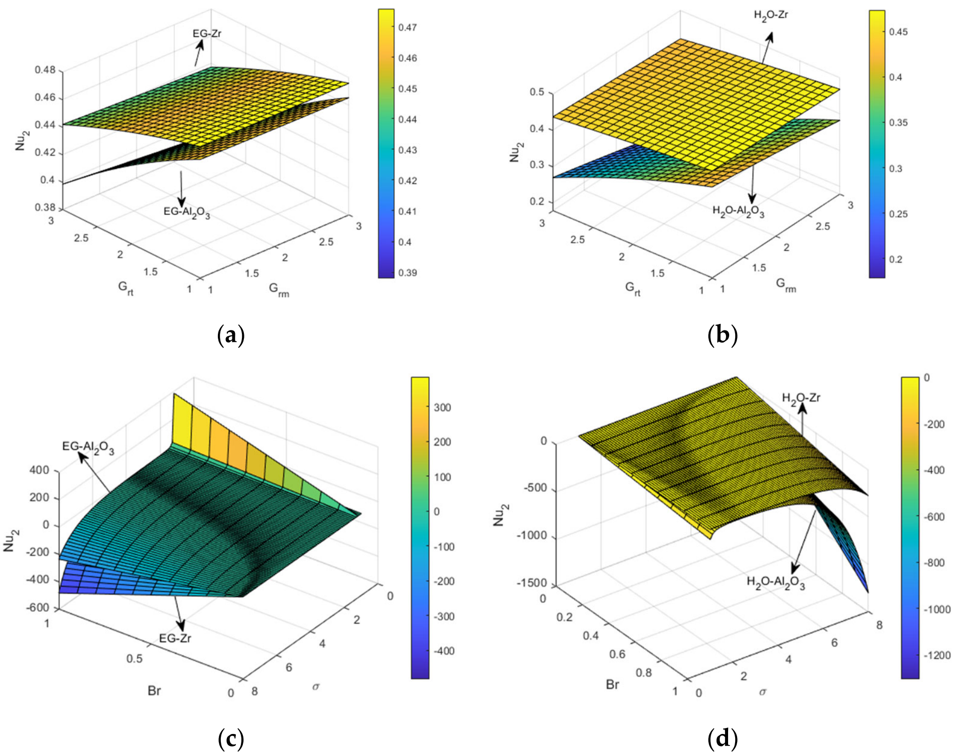

Figure 18. The variation in Nusselt number at lower plate (**a**) G_{rt} and G_{rm} with EG, (**b**) G_{rt} and G_{rm} with H_2O, (**c**) Br and σ with EG, (**d**) Br and σ with H_2O.

Figure 19a,b depict the variation in the skin friction coefficient for different values of G_{rt} and G_{rm}. We can see from both graphs that $EG - Zr$ nanofluids have higher shear stress than other types of particles. Skin friction actually causes flow resistance. That means it is the result of the viscosity of the fluid through which it passes. Since EG is a highly viscous fluid, it experiences greater shear stress. Further, the effect Br and σ is visualized in Figure 19c,d. Here, skin friction is higher for $H_2O - Zr$ nanofluid. It also noted that the rate of shear stress is very low for $EG - Al_2O_3$ nanofluid. Moreover, for higher values of σ, the skin friction coefficient decreased for EG-based nanofluids while increasing for H_2O based nanofluids. Figure 20a–d denote the effects of G_{rt},G_{rm},Br, and σ on the skin friction coefficient at the lower plate, respectively. At the lower plate, the shear stress is high for the $H_2O - Zr$ nanofluid and low for the $EG - Al_2O_3$ nanofluid due to the increasing values of G_{rt} and G_{rm}. A similar effect is observed for varying values of Br and σ. However, the magnitude of improvement is significant when compared to G_{rt} and G_{rm}.

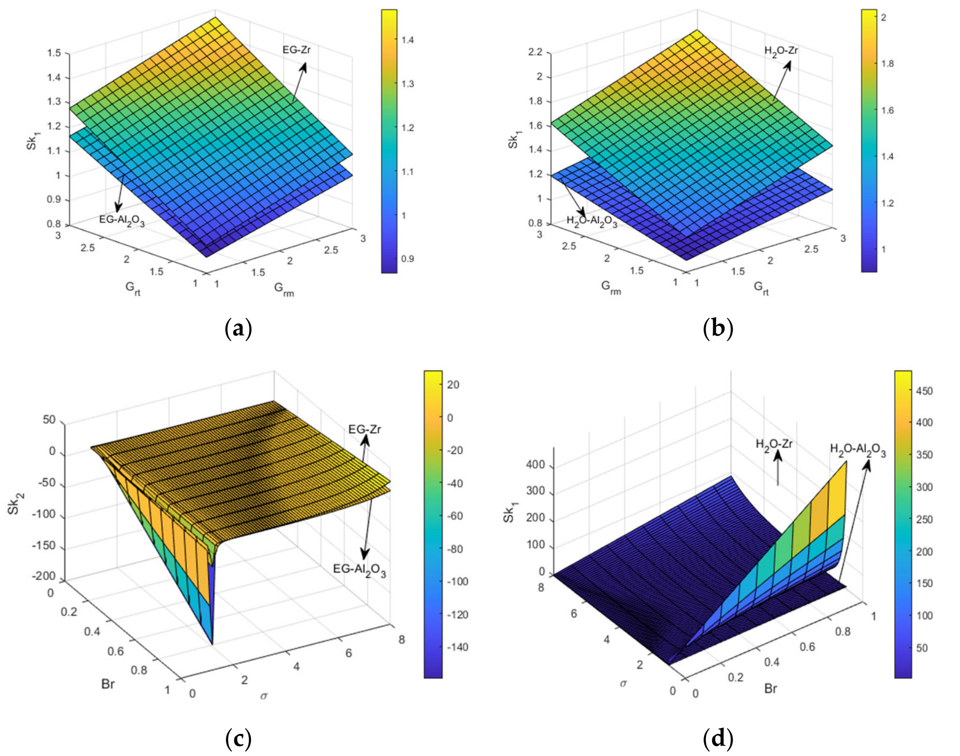

Figure 19. The variation in skin friction at upper plate (**a**) *Grt* and G_{rm} with *EG*, (**b**) *Grt* and G_{rm} with H_2O, (**c**) *Br* and σ with *EG*, (**d**) *Br* and σ with H_2O.

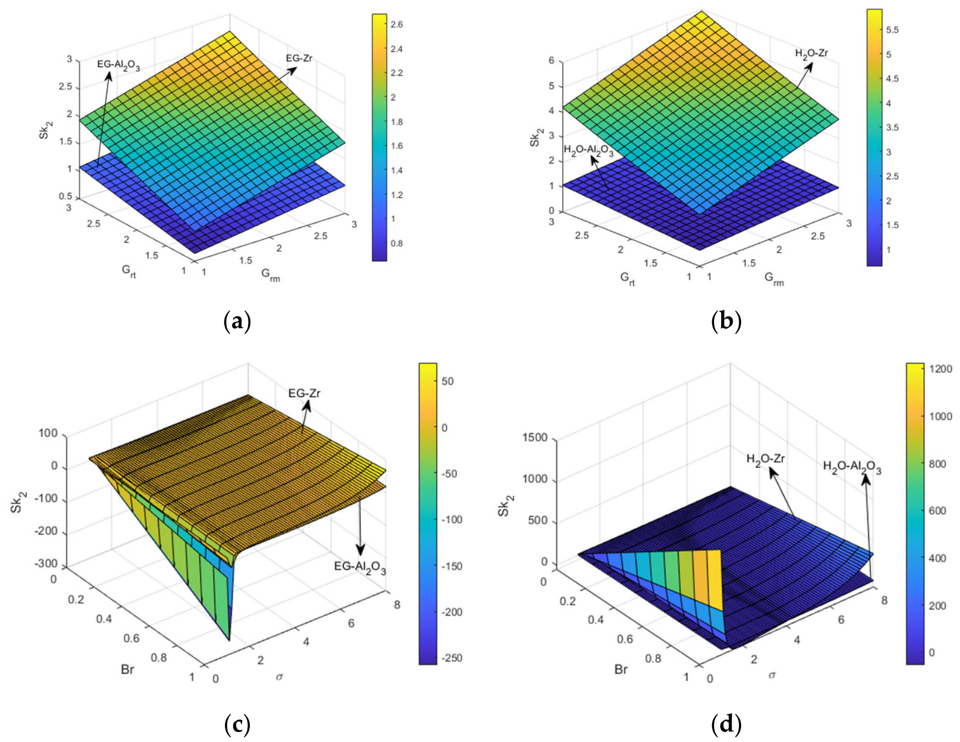

Figure 20. The variation in skin friction at lower plate (**a**) G_{rt} and G_{rm} with *EG*, (**b**) G_{rt} and G_{rm} with H_2O, (**c**) *Br* and σ with *EG*, (**d**) *Br* and σ with H_2O.

5. Validation of Results

In the absence of different parameters, we compared our results with Kumar et al. [45] and Malashetty et al. [46].

For $R = 0$, $\sigma \to 0$, $\alpha = 0$(angle of inclination) and by replacing $P_1 = P_2 = P$, $\phi_1 = \phi_2 = 0$,$f = f_1$ $nf = f_2$ in the governing equations and boundary conditions (1)–(7) of the present paper, our results coincide with the corresponding boundary and interface conditions (2.1)–(2.7) of Kumar et al. [45]. Table 2 demonstrates the effect of Br on temperature with $G_{rt} = 1$, $G_{rm} = 1$, $Kr = 1$, $Sc = 1$, $P = 1$, and $Br = 0, 0.5$, values which are in good agreement with Kumar et al. [31]. Further, this table comprises the perturbation method and FDM (finite difference method) solutions. The percentage of error occurs when $Br = 0.5$. Our results are in excellent agreement with perturbation method solutions.

Table 2. Comparison table of temperature for $Br = 0, 0.5$.

	Temperature					
y	*Br* = 0			*Br* = 0.5		
	Present	Kumar et al. [45]		Present	Kumar et al. [45]	
		PM	FDT		PM	FDT
−1	0.0000	0.0000	0.0000	0.0000	0.0000	0.0000
−0.8	0.1000	0.1000	0.1000	0.1759	0.1790	0.1937
−0.6	0.2000	0.2000	0.2000	0.3282	0.3219	0.3444
−0.4	0.3000	0.3000	0.3000	0.4481	0.4407	0.4664
−0.2	0.4000	0.4000	0.4000	0.5437	0.5459	0.5724
0	0.5000	0.5000	0.5000	0.6489	0.6458	0.6723
0.2	0.6000	0.6000	0.6000	0.7410	0.7447	0.7711
0.4	0.7000	0.7000	0.7000	0.8499	0.8421	0.8678
0.6	0.8000	0.8000	0.8000	0.9355	0.9303	0.9535
0.8	0.9000	0.9000	0.9000	0.9950	0.9924	1.0084
1	1.0000	1.0000	1.0000	1.0000	1.0000	1.0000

Similarly, the governing equations and boundary conditions Equations (1)–(7) of Regions I and II of the present paper coincide with the corresponding governing equations and boundary conditions in Equations (5)–(10) of Regions II and I, respectively, of Malashetty et al. [46], in the absence of the radiation parameter and chemical reaction with $P_1 = P$, $\phi = 0$, and subscripts $f = 1$ and $nf = 2$. Additionally, Figure 21 displays the impact Grt on temperature for $\sigma = 5$, which is identical to Figure 6 from Malashetty et al. [46].

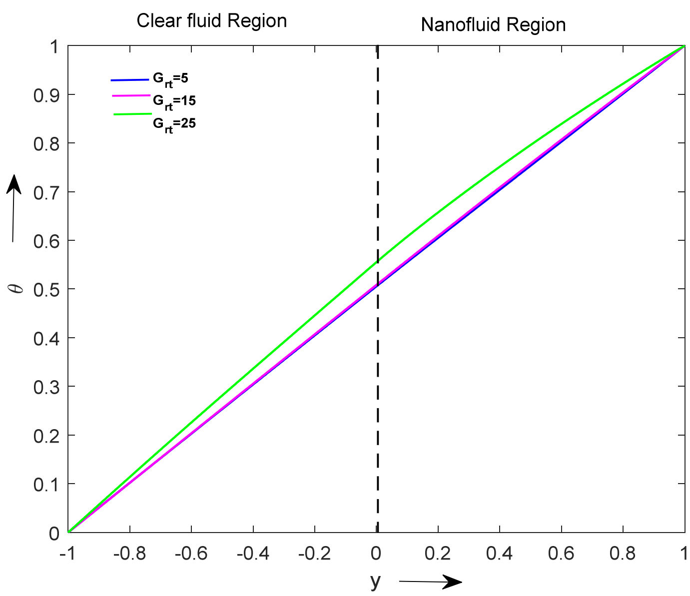

Figure 21. The effect of G_{rt} on temperature for $\sigma = 5$.

6. Conclusions

The current study explores the impacts of thermal radiation and species diffusion on an incompressible steady flow of clear viscous fluid and nanofluids in an inclined channel. A regular perturbation technique was used to solve the problem. The effects of various entrenched parameters on concentration, temperature, and velocity distributions are studied. The following are the conclusions drawn from the results:

- The fluid temperature rises with an increase in the values of G_{rm}, G_{rt} and Br, while it reduces due to an increase in the values of R, α and ϕ. The enhancement of temperature is at its maximum in $H_2O - Zr$ rather than in $EG - Al_2O_3$. Therefore, buoyancy forces dominate the temperature enhancement;
- The rise in the values of Kr and Sc results in subdued concentration fluid; in turn, it increases the species diffusion in the medium;
- The velocity was found to be enhanced for raising values of G_{rm}, G_{rt} and Br in the clear fluid region rather than in the nanofluid region;
- In the presence of solute buoyancy force, in all the profiles of velocity for increasing values of G_{rm} in Region I, the velocity first increases, and at the interface, it exhibits a minor increase; then, they meet at a specific point $y \approx 0.3$ in the Region II, and then a reverse phenomenon is observed;
- For increasing values of σ and ϕ the velocity showing reducing nature in both the regions and found to be more in the nanofluid region;
- In all the cases, the enhancement of temperature was found to be optimal in the case of Zr nanoparticles with water as the base fluid, while a minimum can be observed for Al_2O_3 with ethylene glycol as the base fluid in the nanofluid region. So, ethylene glycol acts as a cooling agent;
- The velocity was found to be maximum in the nanofluid region for $H_2O - Zr$ and minimum for $EG - Al_2O_3$;
- The rate of heat transfer increases at $y = -1$ for water-based nanofluids and decreases for EG-based nanofluids while decreasing at the right boundary for all the varying parameters in both nanofluids;
- The skin friction coefficient increases at the left boundary for EG-based nanofluids and decreases for water-based nanofluids with increasing values of G_{rm}, G_{rt} and Br while it decreases at the right plate;
- The presence of a chemical reaction reduces the fluid concentration;
- The base fluids have the capacity to boost heat transfer intensity by incorporating nanoparticles into them.

Author Contributions: Conceptualization, S.V.K.V. and W.A.-K.; Methodology, S.S.K.R. and S.V.K.V.; Software, K.M.P. and B.N.H.; Validation, B.N.H.; Investigation, S.S.K.R.; Resources, K.M.P.; Data curation, B.N.H.; Writing—original draft, K.M.P.; Writing—review & editing, N.M. and H.M.; Supervision, S.S.K.R., S.V.K.V., H.M. and W.A.-K.; Project administration, W.A.-K.; Funding acquisition, N.M. and H.M. All authors have read and agreed to the published version of the manuscript.

Funding: This work was supported by the research seed grant ref no: RU: EST:MT:2022/3 funded by REVA University.

Institutional Review Board Statement: Not applicable.

Informed Consent Statement: Not applicable.

Data Availability Statement: Not applicable.

Conflicts of Interest: The authors declare no conflict of interest.

Nomenclature

$k-$Thermal conductivity
$\phi-$Solid volume fraction
$\beta-$Coefficient of thermal expansion
β_c-Coefficient of solutal expansion
$g-$Acceleration due to gravity
$u\prime-$Velocity of the fluid
k^*—Mean absorption coefficient
σ^*-Stefan–Boltzmann constant
q_r-Radiative heat flux
$\mu-$Viscosity
$Br-$Brinkman number
$K-$Permeability
$\sigma-$Porosity
$\alpha-$Angle of inclination
$G_{rt}-$Thermal Grashof number
$G_{rm}-$Solute Grashof number
$R-$Radiation parameter
Subscripts:
$f-$Fluid
$nf-$Nanofluid
$s-$Solid
$f-$Fluid

References

1. Maxwell, J.C. *A Treatise on Electricity and Magnetism*; Clarendon Press: Oxford, UK, 1873.
2. Choi, S.U.S.; Eastman, J.A. Enhancing Thermal Conductivity of Fluids with Nanoparticles, Argonne National Lab. (ANL), Argonne, IL (United States), ANL/MSD/CP-84938; CONF-951135-29, October 1995. Available online: https://www.osti.gov/biblio/196525 (accessed on 4 February 2023).
3. Teletov, S.G. On the problem of fluid dynamics of two-phase mixtures, I. Hydrodynamic and energy equations. *Bull. Mosc. Univ.* **1958**, *2*, 15.
4. Joseph, D.D.; Nguyen, K.; Beavers, G.S. Non-uniqueness and stability of the configuration of flow of immiscible fluids with different viscosities. *J. Fluid Mech.* **1984**, *141*, 319–345. [CrossRef]
5. Lohrasbi, J.; Sahai, V. Magnetohydrodynamic heat transfer in two-phase flow between parallel plates. *Flow Turbul. Combust.* **1988**, *45*, 53–66. [CrossRef]
6. Malashetty, M.S.; Leela, V. Magnetohydrodynamic heat transfer in two phase flow. *Int. J. Eng. Sci.* **1992**, *30*, 371–377. [CrossRef]
7. Malashetty, M.S.; Umavathi, J.C.; Kumar, J.P. Magnetoconvection of two-immiscible fluids in vertical enclosure. *Heat Mass Transf.* **2006**, *42*, 977–993. [CrossRef]
8. Vafai, K.; Tien, C.L. Boundary and inertia effects on flow and heat transfer in porous media. *Int. J. Heat Mass Transf.* **1981**, *24*, 195–203. [CrossRef]
9. Vajravelu, K.; Arunachalam, P.V.; Sreenadh, S. Unsteady flow of two immiscible conducting fluids between two permeable beds. *J. Math. Anal. Appl.* **1995**, *196*, 1105–1116. [CrossRef]
10. Kuznetsov, A.V. Analytical investigation of heat transfer in Couette flow through a porous medium utilizing the Brinkman-Forchheimer-extended Darcy model. *Acta Mech.* **1998**, *129*, 13–24. [CrossRef]
11. Cimpean, D.S.; Pop, I. Fully developed mixed convection flow of a nanofluid through an inclined channel filled with a porous medium. *Int. J. Heat Mass Transf.* **2012**, *55*, 907–914. [CrossRef]
12. Ahmad, S.; Pop, I. Mixed convection boundary layer flow from a vertical flat plate embedded in a porous medium filled with nanofluids. *Int. Commun. Heat Mass Transf.* **2010**, *37*, 987–991. [CrossRef]
13. Chamkha, A.J. Flow of Two-immiscible fluids in porous and nonporous channels. *J. Fluids Eng.* **2000**, *122*, 117–124. [CrossRef]
14. Yadav, P.K.; Jaiswal, S.; Sharma, B.D. Mathematical model of micropolar fluid in two-phase immiscible fluid flow through porous channel. *Appl. Math. Mech.* **2018**, *39*, 993–1006. [CrossRef]
15. Umavathi, J.C.; Liu, I.-C.; Kumar, J.P. Magnetohydrodynamic Poiseuille-Couette Flow and Heat Transfer in an Inclined Channel. *J. Mech.* **2010**, *26*, 525–532. [CrossRef]
16. Dogonchi, A.S.; Ganji, D.D. Impact of Cattaneo–Christov heat flux on MHD nanofluid flow and heat transfer between parallel plates considering thermal radiation effect. *J. Taiwan Inst. Chem. Eng.* **2017**, *80*, 52–63. [CrossRef]
17. Umavathi, J.C.; Bég, O.A. Effects of thermophysical properties on heat transfer at the interface of two immisicible fluids in a vertical duct: Numerical study. *Int. J. Heat Mass Transf.* **2020**, *154*, 119613. [CrossRef]

18. Dawar, A.; Saeed, A.; Kumam, P. Magneto-hydrothermal analysis of copper and copper oxide nanoparticles between two parallel plates with Brownian motion and thermophoresis effects. *Int. Commun. Heat Mass Transf.* **2022**, *133*, 105982. [CrossRef]
19. Aleem, M.; Asjad, M.I.; Shaheen, A.; Khan, I. MHD Influence on different water based nanofluids (TiO_2, Al_2O_3, CuO) in porous medium with chemical reaction and newtonian heating. *Chaos Solitons Fractals* **2020**, *130*, 109437. [CrossRef]
20. Esmaeilpour, M.; Korzani, M.G. Enhancement of immiscible two-phase displacement flow by introducing nanoparticles and employing electro- and magneto-hydrodynamics. *J. Pet. Sci. Eng.* **2021**, *196*, 108044. [CrossRef]
21. Narahari, M.; Raju, S.S.K.; Pendyala, R. Unsteady natural convection flow of multi-phase nanofluid past a vertical plate with constant heat flux. *Chem. Eng. Sci.* **2017**, *167*, 229–241. [CrossRef]
22. Santhosh, H.B.; Mahesha; Raju, S.S.K.; Raju, C.S.K. Comparative study on MHD CARREAU fluid due to stretching/shrinking surface in suspension of dust and graphene nanoparticles. *Bionanoscience* **2019**, *9*, 483–494. [CrossRef]
23. Shah, N.A.; Alrabaiah, H.; Vieru, D.; Yook, S.-J. Induced magnetic field and viscous dissipation on flows of two immiscible fluids in a rectangular channel. *Sci. Rep.* **2022**, *12*, 39. [CrossRef] [PubMed]
24. Yadav, P.K.; Kumar, A. An inclined magnetic field effect on entropy production of non-miscible Newtonian and micropolar fluid in a rectangular conduit. *Int. Commun. Heat Mass Transf.* **2021**, *124*, 105266. [CrossRef]
25. Zeeshan, A.; Shehzad, N.; Atif, M.; Ellahi, R.; Sait, S.M. Electromagnetic flow of SWCNT/MWCNT suspensions in two immiscible water- and engine-oil-based newtonian fluids through porous media. *Symmetry* **2022**, *14*, 406. [CrossRef]
26. Raju, S.S.K. Dynamics of magneto-electric hybrid nanoparticles with chemically reacting and radiated moving plate: Entropy analysis. *Int. Commun. Heat Mass Transf.* **2022**, *138*, 106325. [CrossRef]
27. Elmaboud, Y.A. Two layers of immiscible fluids in a vertical semi-corrugated channel with heat transfer: Impact of nanoparticles. *Results Phys.* **2018**, *9*, 1643–1655. [CrossRef]
28. Hisham, M.D.; Rauf, A.; Vieru, D.; Awan, A.U. Analytical and semi-analytical solutions to flows of two immiscible Maxwell fluids between moving plates. *Chin. J. Phys.* **2018**, *56*, 3020–3032. [CrossRef]
29. Sohail, M.; Nazir, U.; Chu, Y.M.; Al-Kouz, W.; Thounthong, P. Bioconvection phenomenon for the bound ary layer flow of magnetohydrodynamic Carreau liquid over a heated disk. *Sci. Iran.* **2021**, *28*, 1896–1907.
30. Al-Kouz, W.; Abderrahmane, A.; Shamshuddin, M.D.; Younis, O.; Mohammed, S.; Bég, O.A.; Toghraie, D. Heat transfer and entropy generation analysis of water-Fe_3O_4/CNT hybrid magnetic nanofluid flow in a trapezoidal wavy enclosure containing porous media with the Galerkin finite element method. *Eur. Phys. J. Plus* **2021**, *136*, 1184. [CrossRef]
31. Rana, P.; Al-Kouz, W.; Mahanthesh, B.; Mackolil, J. Heat transfer of TiO_2—EG nanoliquid with active and passive control of nanoparticles subject to nonlinear Boussinesq approximation. *Int. Commun. Heat Mass Transf.* **2021**, *126*, 105443. [CrossRef]
32. Al-Kouz, W.; Medebber, M.A.; Elkotb, M.A.; Abderrahmane, A.; Aimad, K.; Al-Farhany, K.; Jamshed, W.; Moria, H.; Aldawi, F.; Saleel, C.A.; et al. Galerkin finite element analysis of Darcy–Brinkman–Forchheimer natural convective flow in conical annular enclosure with discrete heat sources. *Energy Rep.* **2021**, *7*, 6172–6181. [CrossRef]
33. Mahesh, A.; Varma, S.V.K.; Raju, C.S.K.; Babu, M.J.; Vajravelu, K.; Al-Kouz, W. Significance of non-Fourier heat flux and radiation on PEG—Water based hybrid nanofluid flow among revolving disks with chemical reaction and entropy generation optimization. *Int. Commun. Heat Mass Transf.* **2021**, *127*, 105572. [CrossRef]
34. Al-Kouz, W.; Al-Waked, R.; Sari, M.E.; Owhaib, W.; Atieh, A. Numerical study of heat transfer enhancement in the entrance region for low-pressure gaseous laminar pipe flows using Al_2O_3—Air nanofluid. *Adv. Mech. Eng.* **2018**, *10*, 1687814018784410. [CrossRef]
35. Ferhi, M.; Djebali, R.; Al-Kouz, W.; Abboudi, S.; Chamkha, A.J. MHD conjugate heat transfer and entropy generation analysis of MWCNT/water nanofluid in a partially heated divided medium. *Heat Transf.* **2021**, *50*, 126–144. [CrossRef]
36. Rana, P.; Mahanthesh, B.; Mackolil, J.; Al-Kouz, W. Nanofluid flow past a vertical plate with nanoparticle aggregation kinematics, thermal slip and significant buoyancy force effects using modified Buongiorno model. *Waves Random Complex Media* **2021**, 1–25. [CrossRef]
37. Alshare, A.; Al-Kouz, W.; Alkhalidi, A.; Kiwan, S.; Chamkha, A. Periodically fully developed nanofluid transport through a wavy module. *J. Therm. Anal. Calorim.* **2021**, *144*, 779–791. [CrossRef]
38. Alshare, A.; Al-Kouz, W.; Khan, W. Cu-Al_2O_3 Water hybrid nanofluid transport in a periodic structure. *Processes* **2020**, *8*, 285. [CrossRef]
39. Al-Kouz, W.; Mahanthesh, B.; Alqarni, M.; Thriveni, K. A study of quadratic thermal radiation and quadratic convection on viscoelastic material flow with two different heat source modulations. *Int. Commun. Heat Mass Transf.* **2021**, *126*, 105364. [CrossRef]
40. Al-Kouz, W.; Bendrer, B.A.-I.; Aissa, A.; Almuhtady, A.; Jamshed, W.; Nisar, K.S.; Mourad, A.; Alshehri, N.A.; Zakarya, M. Galerkin finite element analysis of magneto two-phase nanofluid flowing in double wavy enclosure comprehending an adiabatic rotating cylinder. *Sci. Rep.* **2021**, *11*, 16494. [CrossRef]
41. Saini, G.; Hanumagowda, B.N.; Mulki, H.; Raju, S.; Varma, S.V.K.; Barghout, K.; Murshid, N.; Al-Kouz, W. Entropy Generation Optimization in Couple Stress Fluid Flow with Variable Viscosity and Aligned Magnetic Field. *Sustainability* **2023**, *15*, 2493. [CrossRef]
42. Umavathi, J.C.; Hemavathi, K. Flow and heat transfer of composite porous medium saturated with nanofluid. *Propuls. Power Res.* **2019**, *8*, 173–181. [CrossRef]

43. Rajeev, A.; Mahanthesh, B. Multilayer flow and heat transport of nanoliquids with nonlinear Boussinesq approximation and viscous heating using differential transform method. *Heat Transf.* **2021**, *50*, 4309–4327. [CrossRef]
44. Eshed, M.; Pol, S.; Gedanken, A.; Balasubramanian, M. Zirconium nanoparticles prepared by the reduction of zirconium oxide using the RAPET method. *Beilstein J. Nanotechnol.* **2011**, *2*, 198–203. [CrossRef] [PubMed]
45. Kumar, J.P.; Umavathi, J.C.; Kalyan, S. Chemical reaction effects on mixed convection flow of two immiscible viscous fluids in a vertical channel. *Open J. Heat Mass Momentum Transf.* **2014**, *2*, 28–46. [CrossRef]
46. Malashetty, M.S.; Umavathi, J.C.; Kumar, J.P. Two fluid flow and heat transfer in an inclined channel containing porous and fluid layer. *Heat Mass Transf.* **2004**, *40*, 871–876. [CrossRef]
47. Tiwari, R.K.; Das, M.K. Heat transfer augmentation in a two-sided lid-driven differentially heated square cavity utilizing nanofluids. *Int. J. Heat Mass Transf.* **2007**, *50*, 2002–2018. [CrossRef]
48. Alazmi, B.; Vafai, K. Analysis of fluid flow and heat transfer interfacial conditions between a porous medium and a fluid layer. *Int. J. Heat Mass Transf.* **2001**, *44*, 1735–1749. [CrossRef]
49. Mahanthesh, B.; Gireesha, B.J.; Gorla, R.S.R. Heat and mass transfer effects on the mixed convective flow of chemically reacting nanofluid past a moving/stationary vertical plate. *Alex. Eng. J.* **2016**, *55*, 569–581. [CrossRef]
50. Brinkman, H.C. The Viscosity of Concentrated Suspensions and Solutions. *J. Chem. Phys.* **1952**, *20*, 571. [CrossRef]
51. Mishra, P.C.; Mukherjee, S.; Nayak, S.K.; Panda, A. A brief review on viscosity of nanofluids. *Int. Nano Lett.* **2014**, *4*, 109–120. [CrossRef]
52. Maxwell, J.C. *Electricity and Magnetism*; Dover: New York, NY, USA, 1954; Volume 2.
53. Ahmad, S.; Ali, K.; Faridi, A.A.; Ashraf, M. Novel thermal aspects of hybrid nanoparticles Cu-TiO_2 in the flow of ethylene glycol. *Int. Commun. Heat Mass Transf.* **2021**, *129*, 105708. [CrossRef]
54. Shahri, M.F.; Sarhaddi, F. Second law analysis for two-immiscible fluids inside an inclined channel in the presence of a uniform magnetic field and different types of nanoparticles. *J. Mech.* **2018**, *34*, 541–549. [CrossRef]
55. Zirconium-Properties-Price-Applications-Production, Material Properties, 8 December 2020. Available online: https://material-properties.org/zirconium-properties-applications-price-production/ (accessed on 4 February 2023).
56. Siegel, R.; Howell, J.R. *Thermal Radiation Heat Transfer*, 3rd ed.; Hemisphere: Washington, DC, USA, 1936.
57. Rosseland, S. *Theoretical Astrophysics*; Oxford University Press: London, UK, 1936.
58. Kataria, H.R.; Patel, H.R. Effects of chemical reaction and heat generation/absorption on magnetohydrodynamic (MHD) Casson fluid flow over an exponentially accelerated vertical plate embedded in porous medium with ramped wall temperature and ramped surface concentration. *Propuls. Power Res.* **2019**, *8*, 35–46. [CrossRef]
59. Chamkha, A.J. MHD flow of a uniformly stretched vertical permeable surface in the presence of heat generation/absorption and a chemical reaction. *Int. Commun. Heat Mass Transf.* **2003**, *30*, 413–422. [CrossRef]